Theoretical and Applied Fracture Mechanics 72 (2014) 50–63

Contents lists available at ScienceDirect

Theoretical and Applied Fracture Mechanics

journal homepage: www.elsevier.com/locate/tafmec

Finite strain fracture of 2D problems with injected anisotropic softening elements

P. Areias [a,*], T. Rabczuk [b], P.P. Camanho [c]

[a] Physics Department, University of Évora, Colégio Luís António Verney, Rua Romão Ramalho, 59, 7002-554 Évora, Portugal
[b] Institute of Structural Mechanics, Bauhaus-University Weimar, Marienstraße 15, 99423 Weimar, Germany
[c] DEMEC, Faculdade de Engenharia, Universidade do Porto, Rua Dr. Roberto Frias s/n, 4200-465 Porto, Portugal

ARTICLE INFO

Article history:
Available online 5 July 2014

Keywords:
Quasi-brittle
Ductile
Finite strain
Anisotropy

ABSTRACT

In the context of plane fracture problems, we introduce an algorithm based on our previously proposed rotation of edges but now including the injection of continuum softening elements directly in the process region. This is an extension of the classical smeared (or regularized) approach to fracture and can be seen as an intermediate proposition between purely cohesive formulations and the smeared modeling. Characteristic lengths in softening are explicitly included as width of injected elements. For materials with process regions with macroscopic width, the proposed method is less cumbersome than the cohesive zone model. This approach is combined with smoothing of the complementarity condition of the constitutive law and the consistent updated Lagrangian method recently proposed, which simplifies the internal variable transfer. Propagation-wise, we use edge rotation around crack front nodes in surface discretizations and each rotated edge is duplicated. Modified edge positions correspond to the crack path (predicted with the Ma-Sutton method). Regularized continuum softening elements are then introduced in the purposively widened gap. The proposed solution has algorithmic and generality benefits with respect to enrichment techniques such as XFEM. The propagation algorithm is simpler and the approach is independent of the underlying element used for discretization. To illustrate the advantages of our approach, yield functions providing particular cohesive behavior are used in testing. Traditional fracture benchmarks and newly proposed verification tests are solved. Results are found to be good in terms of load/deflection behavior.

© 2014 Elsevier Ltd. All rights reserved.

1. Introduction

Discretization methods for computational fracture are typically based on meshfree (cf. [53,51,52]) and finite element methods (cf. [35,19,6,20,7,13,16,15]). With the latter, crack propagation algorithms have been developed in the past two decades with successful results. Existing techniques are typically classified as discrete or continuum-based (including combinations of these):

- Total and partial remeshing approaches [25,32,10,18], versions of local displacement [47,46,41,57,44] (and strain [50,2,58]) enrichments, clique overlaps [38], edges repositioning or edge-based fracture with R-adaptivity [45];
- Element erosion [63], smeared procedures [49], viscous-regularized techniques [37], gradient and non-local continua [60,54];
- Phase-field models based on decoupled optimization (equilibrium/crack evolution) with sensitivity analysis [27].

For finite strain simulations, complete numerical experimentation is crucial for obtaining sound conclusions. A trade-off emerges between algorithm intricacy (required by enrichment methods) and increased number of degrees-of-freedom (caused by remeshing algorithms). However, the adaptation of classical contact and cohesive techniques to deal with enriched elements is somehow redundant. It is worth noting that large amplitude displacements can be dealt (see, e.g. [43]) by extended finite elements (XFEM) if neither contact nor cohesive forces are present. Many examples exist for XFEM with cohesive forces ([7,13]) but the generality of the results is limited by the kinematic assumptions, which are stricter than with remeshing. Recently, we introduced the element injection technique [5], which is completed in this work. Distinctive features of this technique are:

* Corresponding author.
E-mail address: pmaa@uevora.pt (P. Areias).

http://dx.doi.org/10.1016/j.tafmec.2014.06.006
0167-8442/© 2014 Elsevier Ltd. All rights reserved.

- Edge rotation algorithm introduced by the Authors [16] with consistent length determination.
- Insertion of "thick" cohesive elements in the form of regularized continuum elements between the crack faces. Element width is related to the softening characteristic length.
- Specialized damage functions for quasi-brittle problems and yield functions for ductile problems.

The perspective is the one of smeared crack (see Oliver [49]) but with a local remeshing strategy, so that the determination of the correct characteristic length described by Oliver is no longer required. In addition, a perfectly defined crack path is obtained, which is not the case with smeared cracks. For materials with softening and plasticity, such as the Rousselier [55] void-fraction yield function, cohesive laws are not directly applicable, since they require the introduction of a large set of assumptions (unloading, fracture modes, etc) and therefore the present approach is more natural. The paper is organized as follows: Section 2 presents our methodology for finite strains, based on the consistent updated Lagrangian method. Section 3 shows the kinematics and our quasi-brittle model, verified by a small example in Section 4. Section 5 details the ductile damage model (based on the Rousselier yield function) and its integration. Subsequently, two quasi-brittle and two ductile benchmarks are shown in Section 7. Finally, in Section 8, conclusions are drawn concerning our proposed algorithm.

2. Equilibrium for an arbitrary reference configuration

Cauchy equations of equilibrium for a given reference configuration are obtained by manipulation of the spatial version of equilibrium (the derivations for the latter are shown in Ogden [48]). Using standard notation (cf. [64]) we write the spatial version of Cauchy equations as (here, i is the direction index and j is the facet index):

$$\frac{\partial \sigma_{ij}}{\partial x_{p_j}} + b_i = 0 \tag{1}$$

with σ_{ij} $(i,j = 1,2,3)$ being the components of the Cauchy stress in an orthonormed basis and b_i the components of the body force vector. The coordinates x_{p_j} are the spatial, or deformed, coordinates of a given point (p) under consideration. It is implied that (1) is satisfied for a time parameter $t \in [0,T]$ with T being the total time of analysis and for a position $\boldsymbol{x}_p \in \Omega_t$ belonging to the deformed position domain at the time of analysis (here denoted Ω_t). Using symmetry of the Cauchy stress and tensor notation, Eq. (1) can be presented as:

$$\boldsymbol{\nabla} \cdot \boldsymbol{\sigma} + \boldsymbol{b} = \boldsymbol{0} \tag{2}$$

where $\boldsymbol{\nabla} = \frac{\partial}{\partial \boldsymbol{x}_p}$ is the spatial gradient operator. In addition to (2), essential and natural boundary conditions defined in terms of two functions g_i and h_i are required (cf. [40]):

$$u_i = g_i \quad \text{on} \quad \Gamma_{g_i} \tag{3}$$

$$\sigma_{ij} n_j = h_i \quad \text{on} \quad \Gamma_{h_i} \tag{4}$$

where the boundary $\Gamma_t = \partial\Omega_t$ is partitioned in $\Gamma_{\boldsymbol{g}}$ and $\Gamma_{\boldsymbol{h}} : \Gamma_t = \Gamma_{\boldsymbol{g}} \cup \Gamma_{\boldsymbol{h}}$ (the essential and the natural boundaries). In Eq. (4), n_j are the components of outer normal to Γ_t in the spatial configuration. Using the definition of the first Piola–Kirchhoff tensor ($\boldsymbol{P}$) and denoting the deformation gradient as $\boldsymbol{F}$, it is possible to modify the derivatives in (1). Making use of the relation $\boldsymbol{\sigma} = \frac{1}{J}\boldsymbol{P}\boldsymbol{F}^T$ with $J = \det \boldsymbol{F}$ we can write the equilibrium equation in material form as:

$$\frac{\partial P_{ij}}{\partial X_{p_j}} + J b_i = 0 \tag{5}$$

where X_{p_j} are the material, or undeformed, coordinates of a given point under consideration. A direct manipulation of (1) with the use of the second Piola–Kirchhoff stress, $\boldsymbol{S}$, allows writing the alternative material form of equilibrium as:

$$\frac{\partial (F_{ik} S_{kj})}{\partial X_{p_j}} + J b_i = 0 \tag{6}$$

or, using $\boldsymbol{\nabla}_0$ as the material gradient operator (the derivative with respect to $\boldsymbol{X}_p$):

$$\boldsymbol{\nabla}_0 \cdot (\boldsymbol{F}\boldsymbol{S})^T + J\boldsymbol{b} = \boldsymbol{0} \tag{7}$$

The time parameter t is the same in Eqs. (7) and (2). However, the position domain is now $\Omega_0 \equiv \Omega_t|_{t=0}$. Therefore, given (6), the conclusion of arbitrariness of X_{p_j} as reference coordinates allows us to use a reference configuration corresponding to an arbitrary instant t_b and the associated position domain Ω_b. Note that t_b is not necessarily in $[0,T]$. This results in the following generalization of (7):

$$\boldsymbol{\nabla}_b \cdot (\boldsymbol{F}_b \boldsymbol{S}_b)^T + J_b \boldsymbol{b} = \boldsymbol{0} \tag{8}$$

where

$$\boldsymbol{\nabla}_b = \frac{\partial}{\partial \boldsymbol{X}_{pb}} \tag{9}$$

$$\boldsymbol{F}_b = \boldsymbol{\nabla}_b \cdot \boldsymbol{x} \tag{10}$$

$$J_b = \det \boldsymbol{F}_b \tag{11}$$

$$\boldsymbol{S}_b = J_b \boldsymbol{F}_b^{-1} \boldsymbol{\sigma} \boldsymbol{F}_b^{-T} \tag{12}$$

The time parameter t is, in Eq. (8), the same as it was in Eq. (2) and the position domain is in this case $\Omega_b \equiv \Omega_t|_{t=t_b}$. If a given time instance t_a is chosen from the interval $[0,T]$, we can re-write (8) as:

$$\boldsymbol{\nabla}_b \cdot (\boldsymbol{F}_{ab} \boldsymbol{S}_{ab})^T + J_{ab} \boldsymbol{b} = \boldsymbol{0} \tag{13}$$

where $\boldsymbol{F}_{ab} = \boldsymbol{\nabla}_b \cdot \boldsymbol{x}_{pa}$ and $\boldsymbol{S}_{ab}^T = \boldsymbol{S}_{ab}$. This equation will be used in the weak form of equilibrium. A fact worth pointing out is the following: t_a must be an equilibrium instant, in contrast with t_b. This explains why simplification attempts of the equilibrium Eq. (8) by switching $\boldsymbol{F}_{ab}$ for $\boldsymbol{I}$ result in loss of convergence in difficult problems.

3. Kinematics and stress integration

Adopting (13) as the equilibrium equation with time parameters t_a and t_b, stress integration can be used in a form that avoids the polar decomposition at each iteration. In a previous work [7] a rate-independent rotational approach was proposed, but it entails a more complex constitutive algorithm in finite strains. The present derivation can be used to achieve an efficient and robust time-integration scheme for finite plastic strains. In addition, if $t_b = 0$, hyperelastic models can be used directly in the material form (as discussed in detail by [39]). Let us consider three configurations Ω_a, Ω_b and Ω_c (respectively at times $t_a \geqslant t_b \geqslant t_c$). A consistent (and consistently linearized) updated-Lagrangian formulation is derived from (13). The formulation can also be viewed as total Lagrangian, since the strain–displacement matrices are similar in structure to those used in this formulation. The relative deformation gradient between two configurations Ω_a and Ω_b is given by[1]:

$$\boldsymbol{F}_{ab} = \frac{\partial \boldsymbol{x}_{pa}}{\partial \boldsymbol{x}_{pb}} \tag{14}$$

or, using the covariant basis (cf. [17]), the following product is obtained:

$$\boldsymbol{F}_{ab} = \boldsymbol{x}_a^T \boldsymbol{y}_b \tag{15}$$

where

$$\boldsymbol{x}_a = \left(\frac{\partial \boldsymbol{x}_{pa}}{\partial \boldsymbol{\xi}} \right)^T \tag{16}$$

[1] Scalar components of $\boldsymbol{F}_{ab}$ are introduced as $[\boldsymbol{F}_{ab}]_{ij}$ for the ith row and jth column.

contains, as rows, the covariant basis vectors of configuration Ω_a. Curvilinear coordinates ξ are often locally identified with the parent domain coordinates. In addition, $\boldsymbol{y}_a = \boldsymbol{x}_a^{-T}$ contains, as columns, the contravariant basis vectors of the same configuration. The inverse of the deformation gradient is obtained by swapping indices a and b : $\boldsymbol{F}_{ab}^{-1} = \boldsymbol{F}_{ba}$. The Jacobian determinant, using the same notation, is given by:

$$J_{ab} = \det \boldsymbol{F}_{ab} \tag{17}$$

and measures the ratio between the volumes at configurations Ω_a and Ω_b. The spatial covariant metric is defined as:

$$\boldsymbol{m}_{aa} = \boldsymbol{x}_a \boldsymbol{x}_a^T \tag{18}$$

Of course, using the spatial metric we can write the right Cauchy-Green tensor (see [48] for the nomenclature) between two configurations Ω_a and Ω_b directly obtained from its definition (15) as:

$$\boldsymbol{C}_{ab} = \boldsymbol{y}_b^T \boldsymbol{m}_{aa} \boldsymbol{y}_b \tag{19}$$

Stress tensors are also naturally given in relation to two configurations Ω_a and Ω_b. Specifically, using the Cauchy stress tensor ($\boldsymbol{S}_{aa}$ or $\boldsymbol{\sigma}$ in the classical notation) can be obtained from the second Piola–Kirchhoff stress $\boldsymbol{S}_{ab}$ between t_a and t_b[2]:

$$\boldsymbol{S}_{aa} = \frac{1}{J_{ab}} \boldsymbol{F}_{ab} \boldsymbol{S}_{ab} \boldsymbol{F}_{ab}^T \tag{20}$$

Changing the reference configuration from Ω_b to Ω_c by a direct generalization of (20) $\boldsymbol{S}_{ac}$ is obtained:

$$\boldsymbol{S}_{ac} = \frac{J_{ac}}{J_{ab}} \boldsymbol{F}_{cb} \boldsymbol{S}_{ab} \boldsymbol{F}_{cb}^T \tag{21}$$

Power-conjugate quantities involving this definition of stress must be of the form:

$$\dot{w} = \frac{1}{2} \boldsymbol{S}_{ab} : \dot{\boldsymbol{C}}_{ab} \tag{22}$$

$\forall t_a > t_b$. The weak form of equilibrium is given by (the upper triangle indicates a "virtual quantity", as employed by Antman [3]):

$$\underbrace{\frac{1}{2} \int_{\Omega_b} \boldsymbol{S}_{ab} : \overset{\triangle}{\boldsymbol{C}}_{ab} \mathrm{d}\Omega_b}_{\overset{\triangle}{W}_{\text{int}}} = \overset{\triangle}{W}_{\text{ext}} \tag{23}$$

when $t_a > t_b$ and, alternatively,

$$\int_{\Omega_a} \boldsymbol{S}_{aa} : \overset{\triangle}{\boldsymbol{\varepsilon}}_{aa} \mathrm{d}\Omega_a = \overset{\triangle}{W}_{\text{ext}} \tag{24}$$

when $t_a = t_b$. These two forms follow directly from (2) and (13) in the previous section and the application of Green's theorem. The so-called "stress updates" in the sense of approximations for the Lie derivative (see Chapters 7 and 8 of [61]) are typically given as:

$$\boldsymbol{S}_{ab} = \Delta \check{\boldsymbol{S}}_{ab} + \underbrace{\frac{1}{J_{bc}} \boldsymbol{F}_{bc} \boldsymbol{S}_{bc} \boldsymbol{F}_{bc}^T}_{\boldsymbol{S}_{bb}} \tag{25}$$

with $\Delta \check{\boldsymbol{S}}_{ab}$ being the relative constitutive stress[3] and $\boldsymbol{S}_{bb}$ can be interpreted as the "transported" stress, whose source is purely kinematic. The strict total Lagrangian formulation is recovered for $b = c = 0$. When considering plasticity it is convenient for $\Delta \check{\boldsymbol{S}}_{ab}$ to depend on a "strain" measure, which in our case is the relative Green–Lagrange strain:

$$\boldsymbol{E}_{ab} = \frac{1}{2} [\boldsymbol{C}_{ab} + \boldsymbol{I}(2\alpha T_{ab} - 1)] \tag{26}$$

where α is the linear thermal expansion coefficient and T_{ab} is the temperature difference between configurations Ω_a and Ω_b. For completeness, we also show that the back-stresses (here denoted by $\boldsymbol{B}$) are given by a similar update scheme,

$$\boldsymbol{B}_{ab} = \Delta \check{\boldsymbol{B}}_{ab} + \underbrace{\frac{1}{J_{bc}} \boldsymbol{F}_{bc} \boldsymbol{B}_{bc} \boldsymbol{F}_{bc}^T}_{\boldsymbol{B}_{bb}} \tag{27}$$

To create a stress contour map, of course Cauchy stresses are physically meaningful and correspond to $\boldsymbol{S}_{aa}$, calculated as $\boldsymbol{S}_{aa} = \boldsymbol{F}_{ab} \left(\Delta \check{\boldsymbol{S}}_{ab} + \boldsymbol{S}_{bb} \right) \boldsymbol{F}_{ab}^T / J_{ab}$ with the appropriate transformations for a global coordinate system. The proposed approach implies a re-writing of classical $\boldsymbol{F}_e \boldsymbol{F}_p$ plasticity codes to work with time increments (one of such codes is discussed in [14]). The linearization of (23) is straightforward (with fewer operations at the constitutive level than the traditional Kirchhoff-stress/strain rate approach) and follows:

$$\mathrm{d}\overset{\triangle}{W}_{\text{int}} = \frac{1}{2} \int_{\Omega_b} \boldsymbol{S}_{ab} : \mathrm{d}\overset{\triangle}{\boldsymbol{C}}_{ab} \mathrm{d}\Omega_b + \frac{1}{4} \int_{\Omega_b} \mathrm{d}\boldsymbol{C}_{ab} : \mathcal{C} : \overset{\triangle}{\boldsymbol{C}}_{ab} \mathrm{d}\Omega_b \tag{28}$$

The determination of $\boldsymbol{C}_{ab}$ and $\boldsymbol{F}_{ab}$ does not have to be compatible in the sense that since an updated problem is solved when switching from Ω_b to Ω_c as reference configuration, it follows that mixed formulations can be used for $\boldsymbol{C}_{ab}$ and not for $\boldsymbol{F}_{bc}$ in (25). Restrictions to moderate *elastic* strains are of course applicable once b and c do not coincide. The interesting versatility of the present approach is that for hyperelastic materials we can coalesce $b = c = 0$ and the Lagrangian description of hyperelasticity can be used *without* specific conditions and for arbitrarily large strains. Otherwise, it is clear that a Lie derivative of the stress is being implicitly calculated and the proposed algorithm belongs to the non-corotational hypoelastic class of algorithms (discussed in [28]). The following limitations are known to be present with this approach:

- Non-zero energy dissipation for large amplitude closed loading cycles.
- Restriction to elastic isotropy when using elasto-plastic constitutive laws.

3.1. Assumed-strain elements: polar decomposition when reaching convergence

For assumed-strain formulations (required here in plane strain and axisymmetric problems with plasticity), agreement should exist between $\boldsymbol{F}_{ab}$ and $\boldsymbol{C}_{ab}$. Since $\boldsymbol{C}_{ab}$ (or alternatively, $\boldsymbol{E}_{ab}$) has an assumed form (or alternatively, an enhanced form), a long standing issue is the compatibility between $\boldsymbol{C}_{ab}$ and $\boldsymbol{F}_{ab}$, see [24]. With our consistent incremental approach, no requirement for *iterative* polar decomposition exists. However, any mismatch between $\boldsymbol{F}_{ab}$ and $\boldsymbol{F}_{ab}^{\star} = \boldsymbol{R}_{ab} \sqrt{\boldsymbol{C}_{ab}}$ typically grows with the number of time steps. To circumvent this problem, we perform a polar decomposition at the end of each time step and use a kinematic rotation (here denoted as $\boldsymbol{R}_{ab}^{\text{kin}}$) to obtain:

$$\boldsymbol{F}_{ab}|_{n+1} = \boldsymbol{R}_{ab}^{\text{kin}} \sqrt{\boldsymbol{C}_{ab}} \tag{29}$$

The kinematic rotation tensor $\boldsymbol{R}_{ab}^{\text{kin}}$ depends on the element technology adopted. For shells, for example, the Kirchhoff rotation can be used [17]. In this paper, a simple iso-parametric plane stress element is used. Plane strain elements make use of a bubble shape function and continuous pressure (the MINI elements [22]).

[2] As discussed before, $\boldsymbol{S}_{ab}$ can be interpreted as the second Piola–Kirchhoff stress at time t_a relative to the reference configuration at time t_b.

[3] Both elastic and inelastic parts contribute to $\Delta \check{\boldsymbol{S}}_{ab}$.

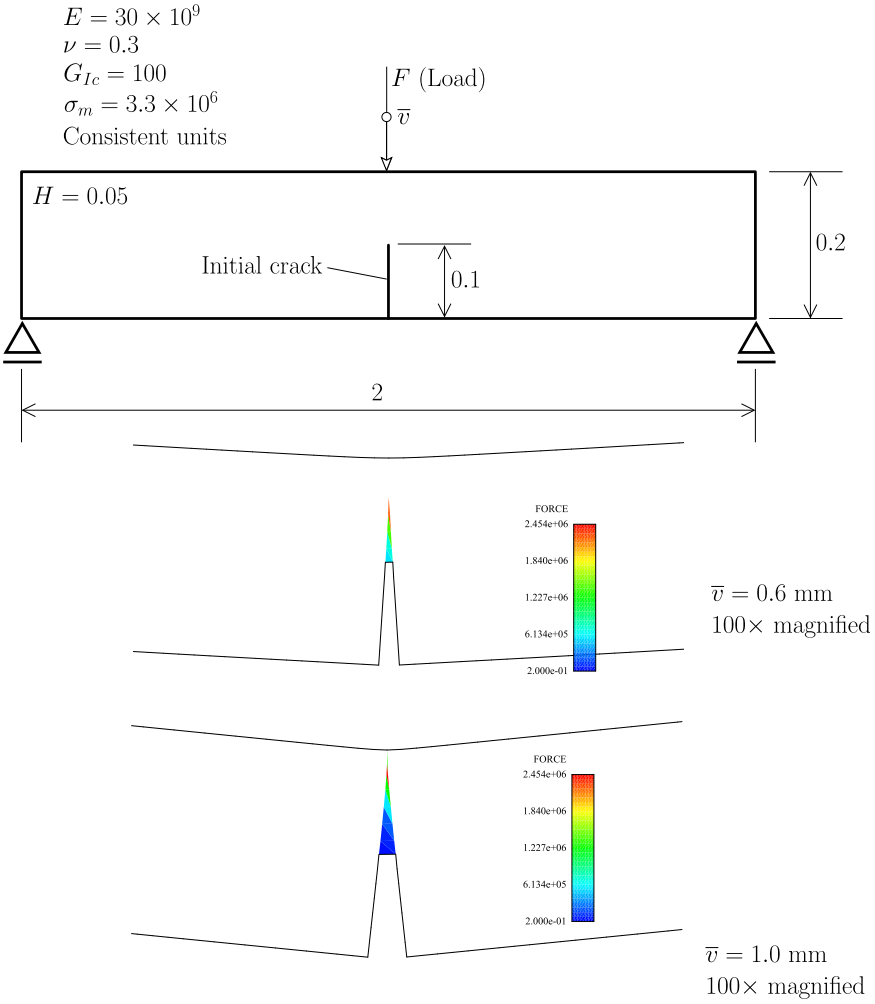

Fig. 1. Verification with the three-point-bending test: relevant data and forces in the cohesive region.

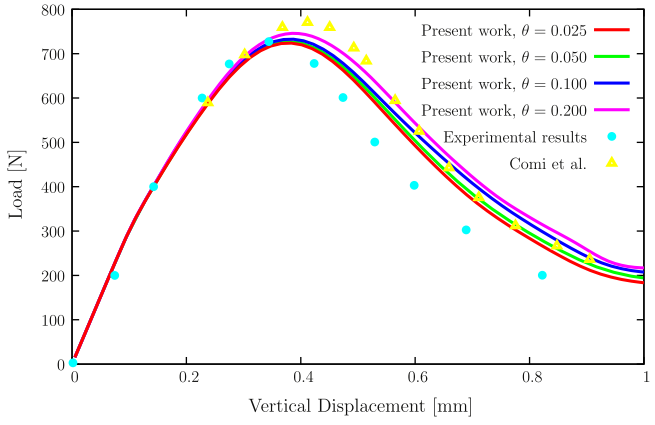

Fig. 2. Effect of θ in the load/displacement results: $\Delta\bar{u}_2 = 5 \times 10^{-3}$, 14,154 initial elements, 7366 initial nodes.

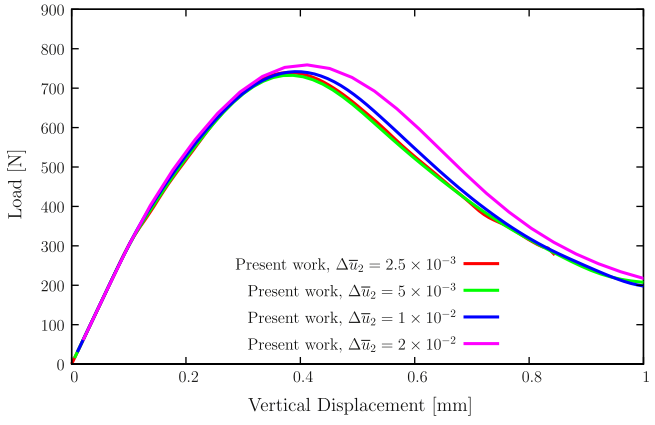

Fig. 3. Effect of $\Delta\bar{u}_2$ in the load/displacement results: $\theta = 0.1$, 14,154 initial elements, 7366 initial nodes.

3.2. Elastic anisotropy: rotation of axes due to motion

For anisotropic materials[4] undergoing finite strains, the definition of the anisotropic axes can occur at a configuration Ω_c. If in this configuration (Ω_c) anisotropic axes are given by the mutually orthogonal directions $\boldsymbol{e}_I^c, \boldsymbol{e}_{II}^c$ and $\boldsymbol{e}_{III}^c$, the corresponding orthogonal matrix is given as:

$$\boldsymbol{R}_c = [\,\boldsymbol{e}_I^c \quad |\boldsymbol{e}_{II}^c \quad |\boldsymbol{e}_{III}^c\,] \tag{30}$$

Since change of reference configuration is accompanied by a change in anisotropic directions, we must include that change in the previ-

[4] Specifically when materials are initially isotropic, so that anisotropy is *induced*.

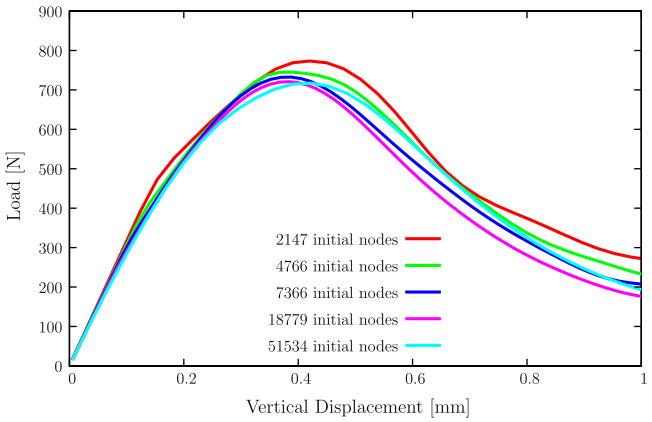

Fig. 4. Effect of number of nodes in the load/displacement results: $\theta = 0.1, \Delta\bar{u}_2 = 5\times 10^{-3}$.

ous framework. This is performed using the polar decomposition of $\boldsymbol{F}_{bc}$:

$$\boldsymbol{R}_b = \boldsymbol{R}_{bc}\boldsymbol{R}_c \tag{31}$$

where $\boldsymbol{R}_{bc}$ is obtained from the exact polar decomposition of $\boldsymbol{F}_{bc}$ and does not require a linearization.

3.3. Quasi-brittle problems: elastic anisotropy

In the thick cohesive elements, we introduce a formulation using a damage variable d such that $d \in [0,1[$. If two consecutive time steps correspond to indices b and a with $t_a \geqslant t_b$, then we can write the relative strain as:

$$\boldsymbol{E}_{ab} = \mathcal{C}^{-1}_{\text{linear}}\left(\frac{\boldsymbol{S}_{ab}}{1-d_a} - \frac{\boldsymbol{S}_{bb}}{1-d_b}\right) \tag{32}$$

where d_b and d_a are the values of d at instants t_b and t_a, respectively. Using $\boldsymbol{S}_{ab} = \chi_a \boldsymbol{S}^{\star}_{ab}$ with $\chi_a = 1-d_a$, we can restrict any norm of $\boldsymbol{S}_{ab}$ by changing d_a. Introducing a loading function Γ as the difference between a function of $\boldsymbol{S}_{ab}$ (here denoted Υ) and a function of a kinematical history variable β (here denoted σ_b)

$$\Gamma = \Upsilon\left(\chi_a \boldsymbol{S}^{\star}_{ab}\right) - \sigma_b(\beta) \tag{33}$$

we can now insert the loading/unloading conditions (often identified as Kuhn-Tucker conditions) as:

$$\Gamma \leqslant 0 \tag{34}$$

$$\Gamma\dot{\beta} = 0 \tag{35}$$

$$\dot{\beta} \geqslant 0 \tag{36}$$

where $\dot{\beta}$ is the time derivative of β. The power conjugacy argument results in the following evolution law for β:

$$\dot{\beta} = \frac{\chi_a \boldsymbol{S}^{\star}_{ab} : \dot{\boldsymbol{E}}_{ab}}{\sigma_b(\beta)} \tag{37}$$

If Υ is a homogeneous function of degree n_d with respect to χ_a, then we can write $\Gamma = \chi_a^{n_d}\Upsilon\left(\boldsymbol{S}^{\star}_{ab}\right) - \sigma_b(\beta)$. Using a fully implicit formulation to determine β and χ_a is not cost effective, since the important quantity in limiting the stresses is χ_a. There are two possible cases: $\Gamma < 0$ (unloading $\dot{\Gamma} < 0$ or reloading $\dot{\Gamma} > 0$) or $\Gamma = 0$ (loading case). The treatment of unloading and reloading is trivial and therefore, for conciseness, we only consider in detail the loading case. Time integration of these constitutive laws is based on the backward-Euler method. Using two time steps b and a we can write:

$$(\beta_a - \beta_b)\sigma_b(\beta_a) - \chi_a \boldsymbol{S}^{\star}_{ab} : \boldsymbol{E}_{ab} = 0 \tag{38}$$

$$\chi_a^{n_d}\Upsilon\left(\boldsymbol{S}^{\star}_{ab}\right) - \sigma_b(\beta_a) = 0 \tag{39}$$

This constitutive system is sufficient to model isotropic damage in (anisotropic) elasticity. The specialization of functions $\sigma_b(\beta)$ and $\Upsilon(\boldsymbol{S}_{ab})$ allows a large variety of behaviors to be modeled. If an extrapolation technique is used for β_a (providing the approximation β_a°), Eqs. (38) and (39) become decoupled. This allows the determination of χ_a:

$$\chi_a = \left[\frac{\sigma_b(\beta_a^{\circ})}{\Upsilon\left(\boldsymbol{S}^{\star}_{ab}\right)}\right]^{\frac{1}{n_d}} \tag{40}$$

Newton iteration for the determination of β_a is therefore given as:

$$\left[\sigma_b(\beta_a) + (\beta_a - \beta_b)\frac{\mathrm{d}\sigma_b(\beta_a)}{\mathrm{d}\beta_a}\right]\delta\beta_a = \chi_a \boldsymbol{S}^{\star}_{ab} : \boldsymbol{E}_{ab} - (\beta_a - \beta_b)\sigma_b(\beta_a) \tag{41}$$

Since we can introduce this law in a thick cohesive element, $\mathcal{C}_{\text{linear}}$ is obtained by transforming a reduced local elasticity matrix $\mathcal{C}_{\text{local}}$ as:

$$\mathcal{C}_{\text{linear}} = \boldsymbol{T}_{\sigma}(\boldsymbol{R})\mathcal{C}_{\text{local}}\boldsymbol{T}_{\varepsilon}(\boldsymbol{R}) \tag{42}$$

where the transformation matrix $\boldsymbol{T}_{\sigma}(\boldsymbol{R})$ is given in general 3D problems as:

$$\boldsymbol{T}_{\sigma}(\boldsymbol{R}) = \begin{bmatrix} R_{11}^2 & R_{21}^2 & R_{31}^2 & 2R_{21}R_{11} & 2R_{31}R_{11} & 2R_{31}R_{21} \\ R_{12}^2 & R_{22}^2 & R_{32}^2 & 2R_{22}R_{12} & 2R_{32}R_{12} & 2R_{32}R_{22} \\ R_{13}^2 & R_{23}^2 & R_{33}^2 & 2R_{23}R_{13} & 2R_{33}R_{13} & 2R_{33}R_{23} \\ R_{11}R_{12} & R_{21}R_{22} & R_{31}R_{32} & R_{21}R_{12}+R_{11}R_{22} & R_{31}R_{12}+R_{11}R_{32} & R_{31}R_{22}+R_{21}R_{32} \\ R_{11}R_{13} & R_{21}R_{23} & R_{31}R_{33} & R_{21}R_{13}+R_{11}R_{23} & R_{31}R_{13}+R_{11}R_{33} & R_{31}R_{23}+R_{21}R_{33} \\ R_{12}R_{13} & R_{22}R_{23} & R_{32}R_{33} & R_{22}R_{13}+R_{12}R_{23} & R_{32}R_{13}+R_{12}R_{33} & R_{32}R_{23}+R_{22}R_{33} \end{bmatrix} \tag{43}$$

with

$$\boldsymbol{R} = [\,\boldsymbol{e}_I \quad |\boldsymbol{e}_{II} \quad |\boldsymbol{e}_{III}\,] \tag{44}$$

where $\boldsymbol{e}_I, \boldsymbol{e}_{II}$ and $\boldsymbol{e}_{III}$ are orthogonal unit vectors corresponding to the directions of fracture modes I, II and III. Transformation matrix $\boldsymbol{T}_{\varepsilon}(\boldsymbol{R})$ is given by:

$$\boldsymbol{T}_{\varepsilon}(\boldsymbol{R}) = \boldsymbol{T}^T_{\sigma}(\boldsymbol{R}^T) \tag{45}$$

This allows the control of elastic anisotropy and therefore pure mode I and combined mixed mode II and III. The full orthotropic elasticity matrix is used, resulting in:

$$\mathcal{C}^{-1}_{\text{local}} = \begin{bmatrix} \frac{1}{E_1} & -\frac{\nu_{21}}{E_2} & -\frac{\nu_{31}}{E_3} & 0 & 0 & 0 \\ -\frac{\nu_{12}}{E_1} & \frac{1}{E_2} & -\frac{\nu_{32}}{E_3} & 0 & 0 & 0 \\ -\frac{\nu_{13}}{E_1} & -\frac{\nu_{23}}{E_2} & \frac{1}{E_3} & 0 & 0 & 0 \\ 0 & 0 & 0 & G_{12}^{-1} & 0 & 0 \\ 0 & 0 & 0 & 0 & G_{13}^{-1} & 0 \\ 0 & 0 & 0 & 0 & 0 & G_{23}^{-1} \end{bmatrix} \tag{46}$$

Symmetry implies $\nu_{ij}E_j = \nu_{ji}E_i, \quad i \neq j$. Specialization for plane stress $\left([\mathcal{C}^{-1}_{\text{local}}]_{\sigma}\right)$ is obvious and for plane strain $\left([\mathcal{C}^{-1}_{\text{local}}]_{\varepsilon}\right)$ a static condensation is performed:

$$[\mathcal{C}^{-1}_{\text{local}}]_{\sigma} = \begin{bmatrix} \frac{1}{E_1} & -\frac{\nu_{21}}{E_2} & 0 \\ -\frac{\nu_{21}}{E_2} & \frac{1}{E_2} & 0 \\ -\frac{\nu_{31}}{E_3} & -\frac{\nu_{32}}{E_3} & 0 \\ 0 & 0 & G_{12}^{-1} \end{bmatrix} \tag{47}$$

$$[\mathcal{C}^{-1}_{\text{local}}]_{\varepsilon} = \begin{bmatrix} \frac{1}{E_1} - \frac{\nu_{31}^2}{E_3} & -\frac{\nu_{21}}{E_2} - \frac{\nu_{31}\nu_{32}}{E_3} & 0 & 0 \\ -\frac{\nu_{21}}{E_2} - \frac{\nu_{31}\nu_{32}}{E_3} & \frac{1}{E_2} - \frac{\nu_{32}^2}{E_3} & 0 & 0 \\ 0 & 0 & 0 & G_{12}^{-1} \end{bmatrix} \tag{48}$$

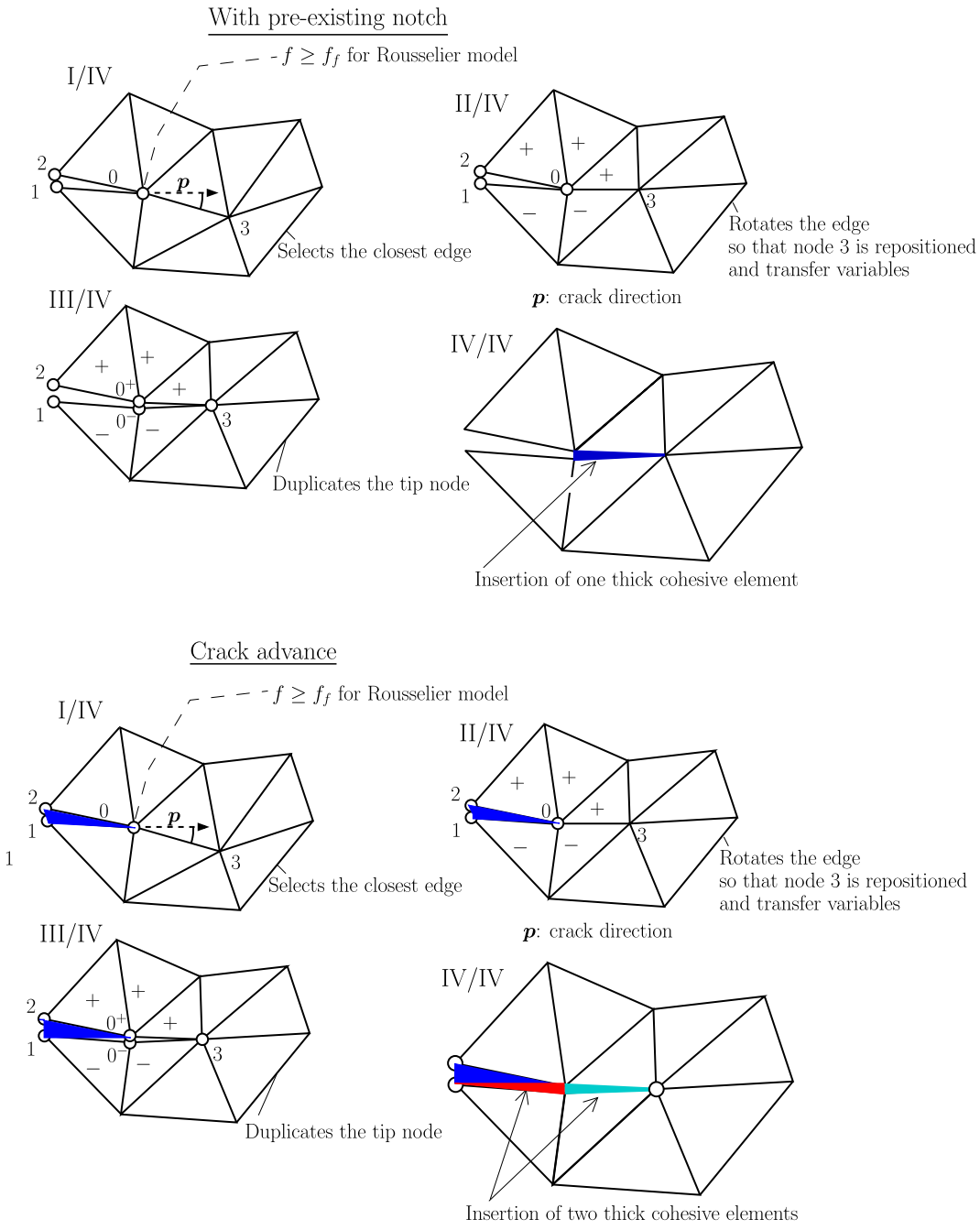

Fig. 5. Edge-based crack propagation algorithm for shells.

The transformation matrix (43) has its dimensions reduced to conform with either case. For an adequate representation of decohesion, matrix $\boldsymbol{R}$ in (44) must be calculated for the configuration Ω_b. For quasi-brittle fracture the following *specific* laws are used:

$$\sigma_b(\beta) = \sigma_m \exp\left(-\beta \frac{\sigma_m l_e}{G_c}\right) \tag{49}$$

$$\Upsilon\left(\boldsymbol{S}^{\star}_{ab}\right) = \arg\max_{s}\left[\det\left(\boldsymbol{S}^{\star}_{ab} - s\boldsymbol{I}\right) = 0\right] \tag{50}$$

The first corresponds to a smooth softening law and the second to the Rankine criterion. A characteristic displacement length corresponding to the fracture energy G_c is obtained by the linear approximation:

$$l_u = \frac{2G_c}{\sigma_m} \tag{51}$$

Since this should be $l_u < l_e$ we must have a characteristic length $l_c = \theta^{-1} l_u$ with $0 < \theta < 1$. In this case, $n_d = 1$. The derivative of χ_a with respect to $\boldsymbol{E}_{ab}$ is given as:

$$\frac{\mathrm{d}\chi_a}{\mathrm{d}\boldsymbol{E}_{ab}} = \begin{cases} -\frac{1}{\Upsilon(\boldsymbol{S}^{\star}_{ab})n_d}\left[\frac{\sigma_b(\beta^{\circ}_a)}{\Upsilon(\boldsymbol{S}^{\star}_{ab})}\right]^{n_d}\left[\frac{\mathrm{d}\Upsilon(\boldsymbol{S}^{\star}_{ab})}{\mathrm{d}\boldsymbol{S}^{\star}_{ab}}\right]\cdot\mathcal{C}_{\text{linear}} & \Gamma = 0 \\ \boldsymbol{0} & \Gamma < 0 \end{cases} \tag{52}$$

The consistent modulus $\mathcal{C}$ is therefore determined as:

$$\mathcal{C} = \boldsymbol{S}^{\star}_{ab} \otimes \frac{\mathrm{d}\chi_a}{\mathrm{d}\boldsymbol{E}_{ab}} + \chi_a \mathcal{C}_{\text{linear}} \tag{53}$$

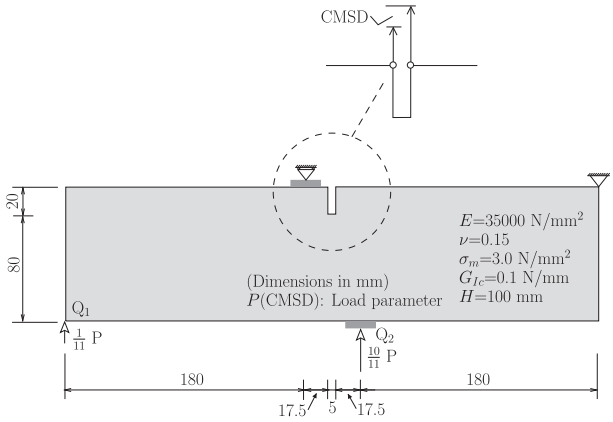

Fig. 6. Schlangen's SEN specimen: relevant data.

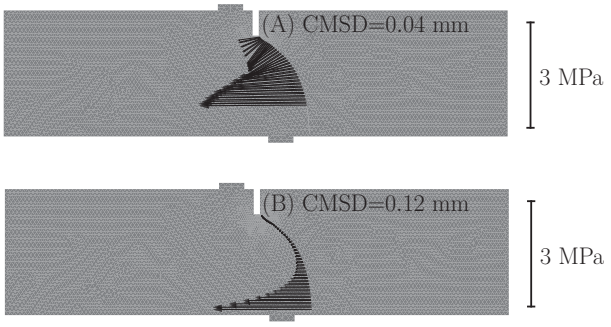

Fig. 8. Cohesive vector tails for two distinct values of CMSD (A and B). Finer mesh is adopted.

In (52), the derivative of $\Upsilon(\boldsymbol{S}^{\star}_{ab})$ with respect to $\boldsymbol{S}^{\star}_{ab}$ is obtained in closed-form by the Acegen software [42].

4. Verification test with a quasi-brittle constitutive law

The classical three-point-bending test, represented in Fig. 1 is employed here for verification. The constitutive law described in subSection 3.3 is used with the following specialization, reproducing a mode I cohesive law:

- $E_1 = E$
- $E_2 = E_3 = 0$

The purpose of this test is to assess the following required non-constitutive data:

- Effect of the non-dimensional characteristic length parameter θ (with values 0.025, 0.050, 0.100 and 0.200).
- Effect of imposed displacement increment $\Delta\bar{u}_2$ (with values 2.5×10^{-3}, 5×10^{-3}, 1×10^{-2} and 2×10^{-2}).
- Effect of mesh size (free triangular meshes with 2147, 4766, 7366, 18,779 and 51,534 nodes).

In Fig. 1, we can also observe two steps with the injected softening elements, for $\bar{v}=0.6$ mm and $\bar{v}=1$ mm. Geometry is 100× magnified. For comparison, we use both numerical and experimental results provided, respectively, by Claudia Comi [33] and co-workers (numerical results) and also the experimental data gathered by Alfaiate and co-workers [1]. Fig. 2 shows the effect of band thickness (in the non-dimensional form θ) in the load/displacement results. Subsequent Figs. 3 and 4 show the effect of the step and mesh size, respectively.

The conclusions that can be drawn from the inspection of Figs. 2–4 are:

- The effect of θ in the load/deflection results is observable, but somehow limited and in-line with the expectable accuracy for fracture problems.
- The effect of step size is observable for large step sizes (in Fig. 3) but subsequent decrease in step size becomes irrelevant.
- Moderate mesh size dependence still exists, but not in a monotonous form, as observed in Fig. 4.

5. Ductile problems with semi-implicit integration

Ductile fracture problems are relevant to test the present approach: non-smooth constitutive laws are adopted, and material history variables are transferred for the thick cohesive elements. In addition, elements in the wake region are forced to unload so that thick cohesive elements localize. It is worth noting that void-fraction based models present problems in terms of integration, which we circumvent here by using a semi-implicit integration with extrapolation of void fraction and effective plastic strain. Using $\dot{\gamma}$ as the plastic strain multiplier, $\boldsymbol{v}$ as the set of history variables

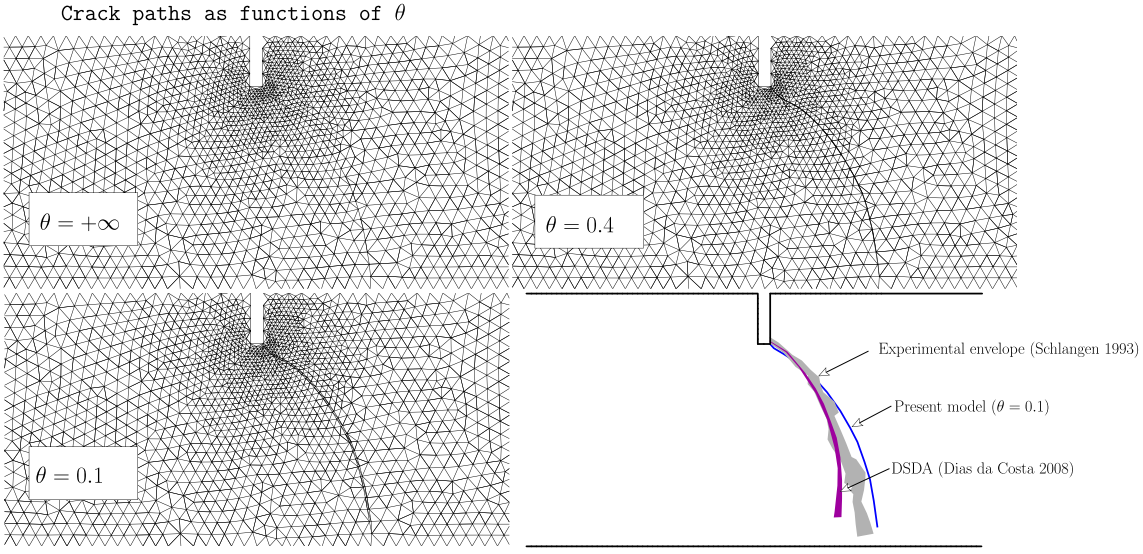

Fig. 7. Schlangen's SEN specimen: crack paths comparison. Crack paths from Schangen [59] and Dias-da-Costa [34] are shown.

for a particular material, $\varphi(\Delta\check{\boldsymbol{S}}_{ab}, \boldsymbol{v})$ as the yield function and $\boldsymbol{n} = \partial\varphi/\partial\Delta\check{\boldsymbol{S}}_{ab}$ as the flow vector, a version of the classical elasto-plastic constitutive system is established. The evolution law for $\boldsymbol{v}$ and the remaining relations are given by:

$$\dot{\boldsymbol{v}} = \dot{\gamma}\boldsymbol{\psi}(\Delta\check{\boldsymbol{S}}_{ab}, \boldsymbol{v}) \tag{54}$$

$$\dot{\gamma} > 0 \tag{55}$$

$$\varphi\left(\Delta\check{\boldsymbol{S}}_{ab}, \boldsymbol{v}\right) > 0 \tag{56}$$

$$\dot{\gamma}\varphi\left(\Delta\check{\boldsymbol{S}}_{ab}, \boldsymbol{v}\right) = 0 \tag{57}$$

$$\dot{\boldsymbol{E}}^p_{ab} = \dot{\gamma}\boldsymbol{n} \tag{58}$$

where $\boldsymbol{\psi}$ is the internal variable function (a thermodynamical approach was recently employed by Areias and Van Goethem [65]). In (54)–(57), $\boldsymbol{\psi}$ is the internal variable evolution function and $\boldsymbol{E}^p_{ab}$ is the relative plastic strain. The implicit integration of the constitutive laws reveals the following residuals $\{\boldsymbol{r}_\varepsilon, r_\gamma, \boldsymbol{r}_v\}$[5]

$$\boldsymbol{r}_\varepsilon = \mathcal{C}^{-1}_{\text{linear}}\Delta\check{\boldsymbol{S}}_{ab} - \boldsymbol{E}_{ab} + \Delta\gamma\boldsymbol{n}(\Delta\gamma, \Delta\check{\boldsymbol{S}}_{ab}, \boldsymbol{v}_r) = \boldsymbol{0} \tag{59}$$

$$r_\gamma = \varphi_c(\Delta\gamma, \Delta\check{\boldsymbol{S}}_{ab}, \boldsymbol{v}_r) = 0 \tag{60}$$

$$\boldsymbol{r}_v = \Delta\boldsymbol{v} - \Delta\gamma\boldsymbol{\psi}(\Delta\gamma, \Delta\check{\boldsymbol{S}}_{ab}, \boldsymbol{v}_r) = \boldsymbol{0} \tag{61}$$

where $\boldsymbol{v} = \{\gamma, \boldsymbol{v}_r\}$. In (61), the function φ_c is given as:

$$\varphi_c = \left\langle \mu\Delta\gamma + \varphi\left(\Delta\gamma, \Delta\check{\boldsymbol{S}}_{ab}\right)\right\rangle - \mu\Delta\gamma \tag{62}$$

where μ is the shear modulus and $\langle\bullet\rangle$ is the ramp function. This is complemented, for plane stress, by the equation $\left[\Delta\check{\boldsymbol{S}}\right]_{33} = 0$, cf. [17]:

$$\Delta E_{33} = \Delta\gamma n_{33} + \frac{1}{\mathcal{C}_{3333}}[\mathcal{C}_{3311}(\Delta\gamma n_{11} - \Delta E_{11}) + \mathcal{C}_{3322}(\Delta\gamma n_{22} - \Delta E_{22})]$$

We further modify the constitutive system with the following combined implicit/extrapolation scheme:

- History variables $\boldsymbol{v}$ are implicitly integrated by the backward-Euler method *after* the first two constitutive equations are satisfied, by applying Newton–Raphson method to the following system:

  $\boldsymbol{v}^\star_a = \boldsymbol{v}^\star_b + \Delta\gamma\boldsymbol{\psi}_a\left(\Delta\gamma, \Delta\check{S}_{ab}, \boldsymbol{v}^\star_a\right)$, noting the dependence of $\boldsymbol{\psi}_a$ on $\boldsymbol{v}^\star_a$.

- Extrapolation from the previous step is adopted for the arguments of $\boldsymbol{n}$ and φ_c:

  $$\boldsymbol{v}_a = \boldsymbol{v}^\star_b + (\Delta t_a/\Delta t_b)(\boldsymbol{v}^\star_b - \boldsymbol{v}^\star_c)$$

where $\boldsymbol{v}^\star$ indicates an implicitly integrated history variable and $\boldsymbol{v}$ indicates an extrapolated history variable.

The reduced constitutive system is now:

$$\boldsymbol{r}_\varepsilon = \mathcal{C}^{-1}_{\text{linear}}\Delta\check{\boldsymbol{S}}_{ab} - \boldsymbol{E}_{ab} + \Delta\gamma\boldsymbol{n}(\Delta\gamma, \Delta\check{\boldsymbol{S}}_{ab}, \boldsymbol{v}_a) = \boldsymbol{0} \tag{63}$$

$$r_\gamma = \varphi_c(\Delta\gamma, \Delta\check{\boldsymbol{S}}_{ab}, \boldsymbol{v}_a) = 0 \tag{64}$$

The system (63) and (64) is solved for $\Delta\check{\boldsymbol{S}}_{ab}$ and $\Delta\gamma$ by means of the Newton–Raphson method, which requires the derivatives of both equations with respect to $\Delta\check{\boldsymbol{S}}_{ab}$ and $\Delta\gamma$. Using the residual $\boldsymbol{r}_c = \{\boldsymbol{r}_\varepsilon, r_\gamma\}^T$ we calculate the Jacobian as:

$$\boldsymbol{J} = \begin{bmatrix} \mathcal{C}^{-1}_{\text{linear}} + \Delta\gamma\frac{\partial\boldsymbol{n}}{\partial\Delta\check{\boldsymbol{S}}_{ab}} & \boldsymbol{n} + \Delta\gamma\frac{\partial\boldsymbol{n}}{\partial\Delta\gamma} \\ \frac{\partial\varphi_c}{\partial\Delta\check{\boldsymbol{S}}_{ab}} & \frac{\partial\varphi_c}{\partial\Delta\gamma} \end{bmatrix} \tag{65}$$

The consistent tangent modulus is defined as:

[5] Note that the system does not correspond to a *return-mapping* approach.

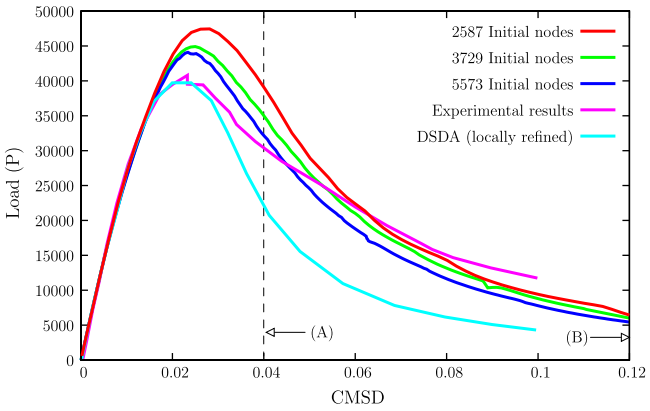

(a) CMSD/load results

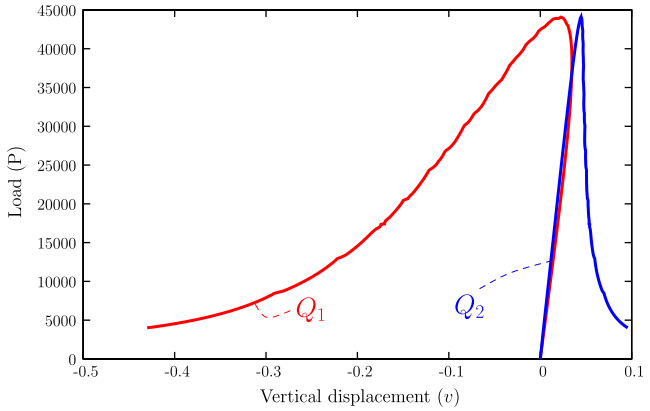

(b) Load (P) versus vertical displacement of points Q_1 and Q_2. Results for the finer mesh are shown.

Fig. 9. CMSD/load results, compared with the experimental results by Schlangen [59] and the DSDA technique [34].

$$\mathcal{C}_{\text{consistent}} = \frac{\partial\Delta\check{\boldsymbol{S}}_{ab}}{\partial\boldsymbol{E}_{ab}} \tag{66}$$

which, of course, is obtained from the Eqs. (63), (64) by performing the elimination for $\Delta\check{\boldsymbol{S}}_{ab}$:

$$\mathcal{C}_{\text{consistent}} = \overline{\mathcal{C}} - \frac{\left[\overline{\mathcal{C}}\left(\boldsymbol{n} + \Delta\gamma\frac{\partial\boldsymbol{n}}{\partial\Delta\gamma}\right)\right] \otimes \left[\left(\frac{\partial\varphi_c}{\partial\Delta\check{\boldsymbol{S}}_{ab}}\right)^T\overline{\mathcal{C}}\right]}{\left(\frac{\partial\varphi_c}{\partial\Delta\check{\boldsymbol{S}}_{ab}}\right)^T\overline{\mathcal{C}}\left(\boldsymbol{n} + \Delta\gamma\frac{\partial\boldsymbol{n}}{\partial\Delta\gamma}\right) - \frac{\partial\varphi_c}{\partial\Delta\gamma}} \tag{67}$$

with

$$\overline{\mathcal{C}} = \left(\mathcal{C}^{-1}_{\text{linear}} + \Delta\gamma\frac{\partial\boldsymbol{n}}{\partial\Delta\check{\boldsymbol{S}}_{ab}}\right)^{-1} \tag{68}$$

5.1. The Rousselier model and its integration

The Rousselier [55] model for ductile damage is characterized by the following yield function in non-dimensional form:

$$\varphi(y, \boldsymbol{S}_{ab}, f_\star) = \frac{\sigma(\boldsymbol{S}_{ab})}{(1-f)y} + \frac{\sigma_1 f}{y}D\exp\left[\frac{\text{tr}[\boldsymbol{S}_{ab}]}{3(1-f)\sigma_1}\right] - 1 = 0 \tag{69}$$

in which f is the void fraction and y is the hardening value, given as a function of ε_p. In addition to the hardening characteristics, the only additional properties are σ_1, D and f_0. The property σ_1 can be *estimated* from the original yield stress, $y_0 = y|_{\varepsilon_p=0}$ and the ultimate tensile strength, $y_{\max} = \max_{\varepsilon_p} y$ as:

$$\sigma_1^{\text{estimate}} = \frac{1}{3}(y_0 + y_{\max}) \tag{70}$$

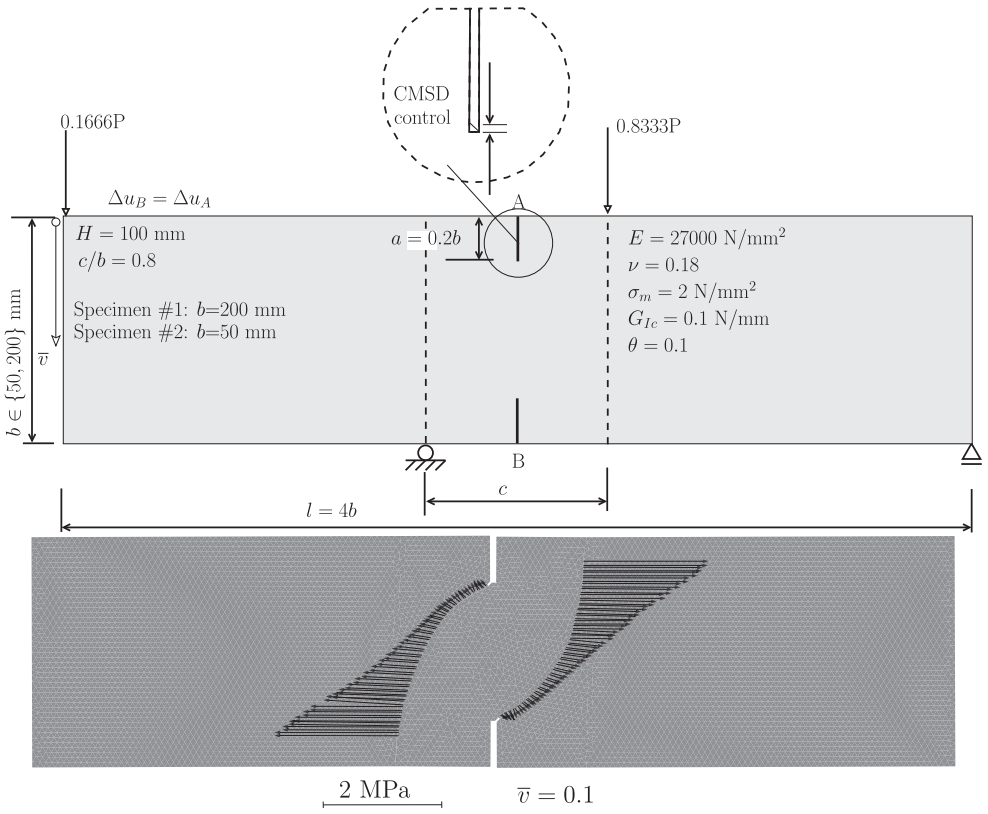

Fig. 10. Four-point bending of a concrete beam: geometry, boundary conditions, multiple point constraints ($\Delta u_B = \Delta u_A$) and material properties. Also shown is the final deformed mesh 10× magnified with the attached cohesive stress vectors.

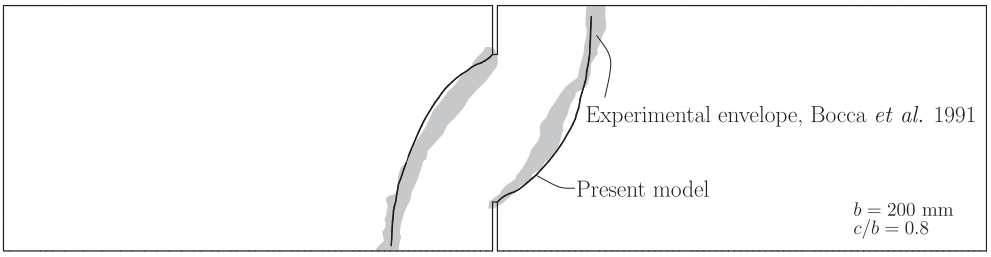

Fig. 11. Four-point bending of a concrete beam: crack paths compared with the envelope of experimental results by Bocca, Carpintieri and Valente [26].

Void fraction follows from volume change and is calculated as

$$f = 1 - (1 - f_0)\exp[-3\varepsilon_m] \tag{71}$$

or, using a linearized version, as

$$f = 1 - (1 - f_0)(1 - 3\varepsilon_m) \tag{72}$$

It can be observed that D indirectly controls the void growth rate. We force the growth near the critical value of void fraction to model initiation as in the GTN model, but with a slight difference:

$$f_\star = f_c + \frac{f_f - f_c}{f_a - f_c}(f - f_c)$$

Typically, $f_c = 0.3$ and $f_f = 0.95$. An initial void fraction f_0 is also assumed. Using Voigt notation, the corresponding deviatoric stress is $\boldsymbol{S}_{ab\prime} = \mathtt{Dev} \cdot \boldsymbol{S}_{ab}$, and $\sigma = \sqrt{3\boldsymbol{S}_{ab\prime} \cdot \boldsymbol{I}_6 \cdot \boldsymbol{S}_{ab\prime}/2}$ is the von-Mises equivalent stress. Here, the Voigt form of $\boldsymbol{I}_6$ is given by:

$$[\boldsymbol{I}_6]_{ij} = \delta_{ij}\left(1 + \sum_{k=1}^{3}\delta_{ik+3}\right) \tag{73}$$

The deviatoric matrix (Dev in the Voigt form) is given by:

$$\mathtt{Dev} = \frac{1}{3}\begin{bmatrix} 2 & -1 & -1 & 0 & 0 & 0 \\ -1 & 2 & -1 & 0 & 0 & 0 \\ -1 & -1 & 2 & 0 & 0 & 0 \\ 0 & 0 & 0 & 3 & 0 & 0 \\ 0 & 0 & 0 & 0 & 3 & 0 \\ 0 & 0 & 0 & 0 & 0 & 3 \end{bmatrix} \tag{74}$$

The equivalent plastic strain increment is computed based on the following power equivalence relation:

$$\boldsymbol{S}_{ab} \cdot \dot{\boldsymbol{\varepsilon}}_p = (1 - f_\star) y \dot{\varepsilon}_p \tag{75}$$

The effective plastic strain rate is given by this power equivalence:

$$\dot{\varepsilon}_p = \frac{\dot{\gamma}}{y(1 - f_\star)}\boldsymbol{S}_{ab} \cdot \boldsymbol{n} \tag{76}$$

Integration of constitutive quantities follow the unconditionally stable backward-Euler scheme:

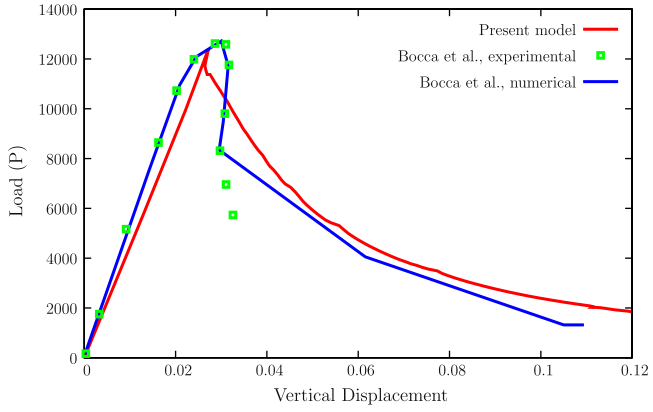

Fig. 12. Load- displacement results, compared with the results of Bocca et al. [26] and the cracking particle method of Rabczuk and Belytschko [53] (for the case $b = 200$ mm) with their 68,000 particle analysis.

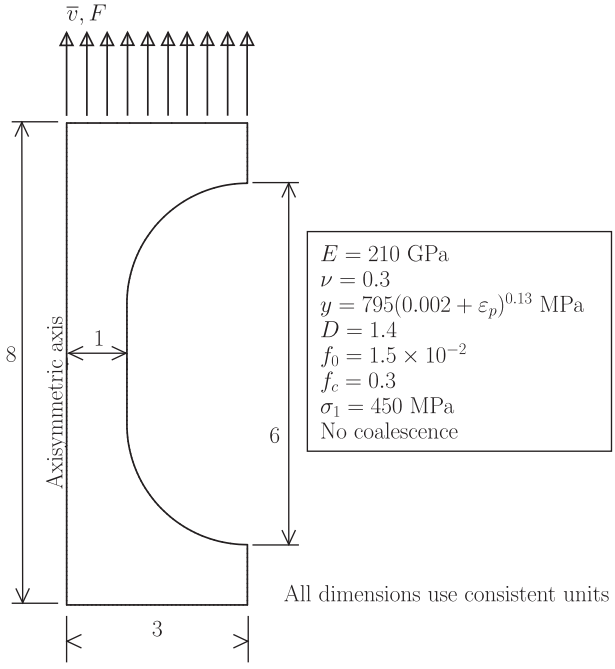

Fig. 13. Besson cylindrical specimen modeled with axisymmetric elements. Relevant data (see also [23]).

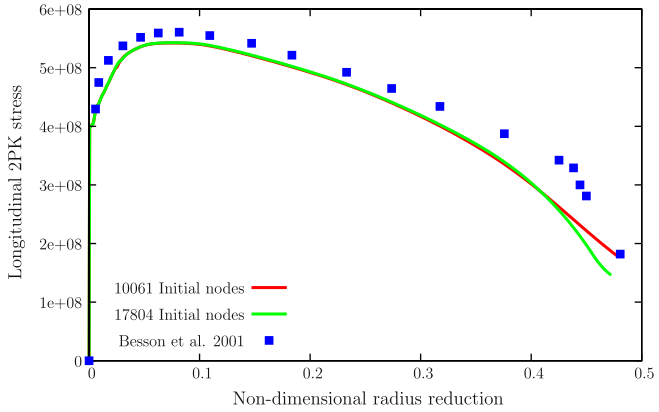

Fig. 14. Besson cylindrical specimen: second Piola–Kirchhoff stress vs. radial reduction, compared with the results of Besson et al. [23].

$$\varepsilon_{p_a} = \varepsilon_{p_b} + \frac{\Delta\gamma}{y_a(1 - f_\star)} \boldsymbol{S}_{ab} \cdot \boldsymbol{n} \tag{77}$$

Time stepping is adapted so that $\Delta\varepsilon_p = \varepsilon_{p_a} - \varepsilon_{p_b}$ is kept below 5%. This measure is necessary for accuracy reasons in problems with localization. The derivation of the derivatives of φ discussed in Section 5 are performed with AceGen [42] and exported to Simplas [4]. Since any equation containing the ramp function $\langle x \rangle$ is non-smooth, the Newton–Raphson method will typically have convergence difficulties or fail to converge, a replacement can be used with convergence advantages. Eterovic and Bathe recognized this in 1991 [36] and used a semi-smooth function. We use the Chen-Mangasarian replacement function ([31,30]) $S(x) \cong \langle x \rangle$, which is smooth in the complete domain, to replace the ramp function. The function depends on an `Error` parameter. In the examples we use a non-dimensional `Error` of 1×10^{-3}. Consequences of this replacement were discussed by Areias and Rabczuk [14].

6. Crack propagation

Crack propagation follows the edge rotation recently introduced by Areias and Rabczuk [15], complemented by the insertion of thick cohesive elements. A Figure depicting this procedure is shown Fig. 5. For the Rousselier model, the criterion is simply the critical void fraction, using the condition:

$$f \geqslant f_f \Rightarrow \text{crack advance} \tag{78}$$

Algorithmic steps for crack propagation steps are (see Fig. 5) the following:

1. A ranking of node tips is performed according to the advance indicator.
2. The crack direction is estimated by Ma-Sutton criterion, considering thick cohesive elements as voids (cf. [62]).
3. At the node tip, the estimated direction is used to select the closest edge.
4. The edge is rotated so that it matches the estimated direction.
5. A duplication of the node tip is performed, creating a new tip (advancing the crack).
6. New thick cohesive elements are inserted.

For ductile problems, where internal variable mapping is necessary, we adopt the following algorithm:

- After step 3, we unload the mesh and set the stresses to zero (retaining all internal variables).
- The remeshing step follows the previous scheme.
- Loading up to the previous value of load or displacement parameter is performed.

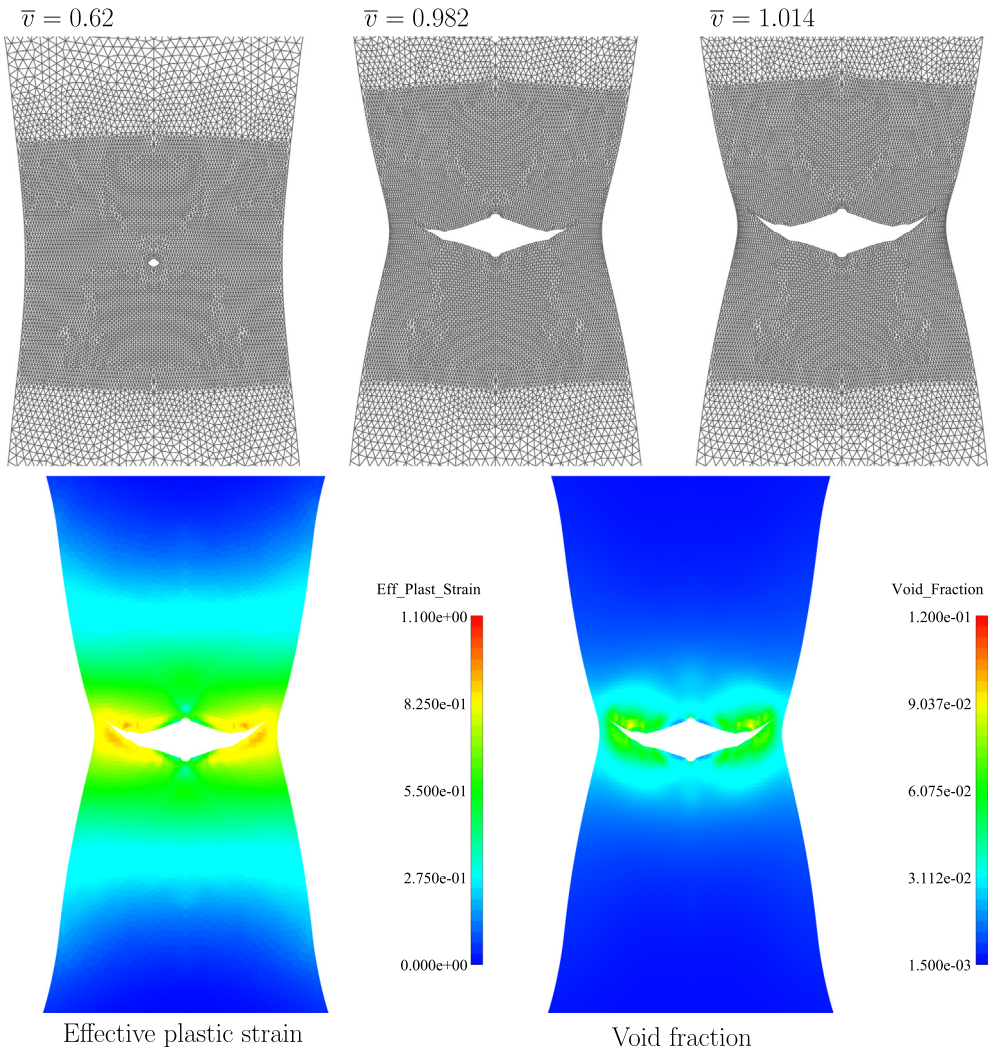

Fig. 15. Besson cylindrical specimen: cup and cone formation and corresponding contour plots (f and ε_p).

7. Numerical examples

7.1. Quasi-brittle single edge-notched beam

This version of the single-edge-notched beam problem was introduced by Schlangen (cf. [59]) and is now modeled. It consists of a pre-notched beam loaded in two points and supported in other two points. Fig. 6 contains the relevant data for this problem. It is appropriate for the assessment of the injection method since the experimentally observed result is a curved crack emanating from the right corner of the notch. Curved cracks are difficult to reproduce with smeared models. Since $\boldsymbol{P}$ cannot be monotonous when crack propagation occurs, a control equation is used, which increases the shear mouth relative displacement of the initial notch (cf. Fig. 6). This is called crack mouth sliding displacement (CMSD) and is, in this paper, imposed at the global level.

We test three triangular meshes containing 2587, 3729 and 5573 nodes. The resulting crack path is not far from the experimental envelope, as can be observed in Fig. 7 (see also Fig. 8); even near the support the experimental observations are reasonably reproduced. A comparison with the experimental results and the DSDA method [1,9], along with a study of mesh size influence is performed. As can be observed in Fig. 9, after the peak load is reached, the numerical results are more brittle than the experimental results. According to Alfaiate, Wells and Sluys [2], this is due to the fact that an isotropic mode-I traction-jump law is used. Since crack paths are nearly insensitive to the value of θ, we fix the value $\theta = 0.2$ for the mesh size effect study.

7.2. Cohesive crack growth in a four-point bending concrete beam

The bi-notched concrete beam proposed by Bocca et al. [26] is tested. The beam is simply supported in two points and subjected to two point loads. The effect of beam size in brittleness is assessed by using two different specimen dimensions. The corresponding experimental setting is described in detail in the original work [26]. From the set of specimens studied by Bocca et al. we retain the specimens, both with $c/b = 0.8$: one with $b = 50$ and another with $b = 200$ mm. These have reported experimental measurements in [26]. We are also concerned with the crack paths that were reported in [26]. Using the well-known cracking particle method, Rabczuk and Belytschko [53] obtained very good results for the crack path prediction, although with a slightly higher load than the experimental one. However, with the particle methods, there is an ambiguity in assigning the support dimension for the crack region. We use a single uniform initial mesh, with 7488 nodes and 14536 triangular elements. All relevant data is shown in Fig. 10. For anti-symmetry reasons, we force the same mouth horizontal displacement at the edge of notches A and B: $\Delta u_B = \Delta u_A$. It has been debated if quasi-static simulations allow propagation of more than one crack (concerning this topic, see the excellent thesis by Chaves [29]), and the imposition of same

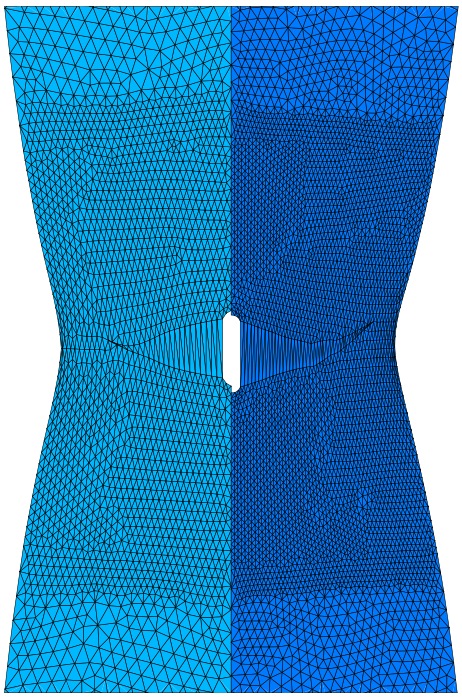

Fig. 16. Crack path formation: comparison between 10,061 and 17,804 initial nodes.

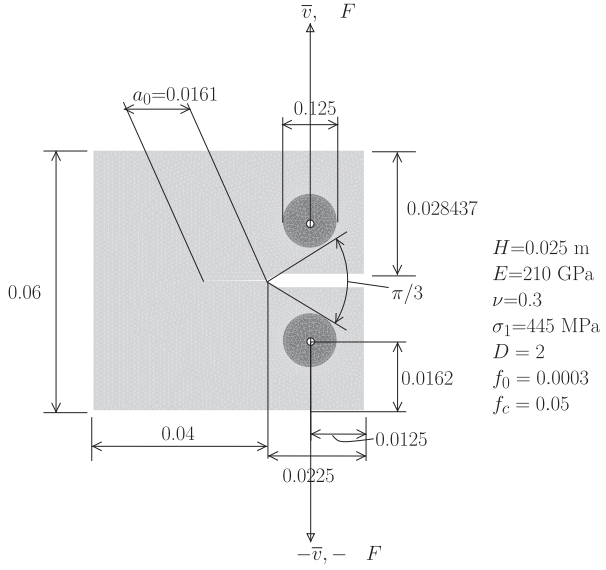

Fig. 17. Compact tension specimen. Lengths given in meters. The hardening function is provided in [56].

Table 1
Hardening law used in the compact tension specimen (Fig. 17).

ε_p	y (MPa)
0	405
0.0568	569
0.0710	584
0.0994	621
0.1207	634
0.1917	675
0.2864	721
0.5089	796
0.8260	881
1.1030	935

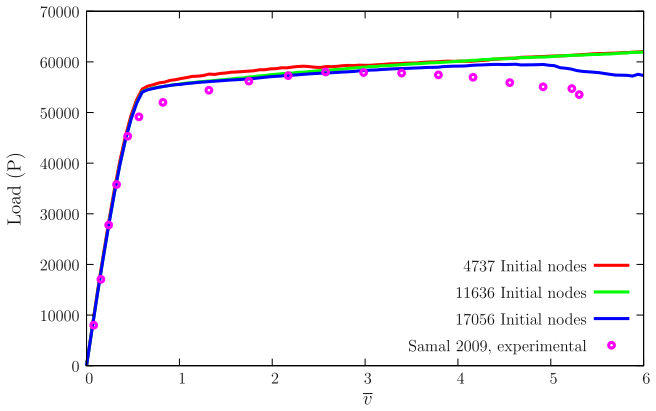

Fig. 18. Compact tension specimen: comparison between experimental (reported in [56]) and numerical results for three different initial meshes.

relative displacement forces both cracks to evolve simultaneously. We obtain an excellent agreement with the experimental crack paths, as shown in Fig. 11. The relatively wide spread of experimental crack paths is typical and is a consequence of the use of 6 specimens of reference [26]. Experimentally, some residual crack evolution in the opposite direction of the final path was observed and we also obtained that effect. Load–displacement results are shown in Fig. 12 where a comparison with the measurements of Bocca et al. [26] and the cracking particle method of Rabczuk and Belytschko [53] is made. For the smaller specimen there is a somehow longer and lower curve than the observed one.

7.3. Cup and cone fracture

A tension test producing cup and cone fracture was described by Besson [23] and is here reproduced. We include explicit crack propagation by element injection subsequently to the satisfaction of $f \geqslant f_f$. Fig. 13 (see Fig. 14 for a comparison with results by Besson) shows relevant data for this problem. The stress/displacement results are compared with results obtained by Besson et al. [23]. We are also concerned with the cup and cone formation, which requires a sufficiently refined mesh and elongated elements in the radial direction. Fig. 15 shows the crack formed in the necking region and propagating toward the outer surface, forming the cup and cone. This type of result, combining the localization in ductile materials and a physically meaningful ductile crack formation is very rare in the literature. In addition, robustness is an advantage when compared with GFEM/XFEM. The stress/displacement results are compared with results obtained by Besson et al. [23]. Crack path formation is compared between the two meshes in Fig. 16. Some differences can be observed in the crack path, but these results are in-line with what is expected from crack propagation analysis with ductile materials.

7.4. Compact tension specimen

The compact tension specimen described by Samal et al. [56] is reproduced. In that paper, the Rousselier yield function was adopted to model ductile fracture of a pre-cracked ($a_0 = 0.0161$ m) specimen. Experimental results were also reported. The Authors used a gradient model to attenuate the mesh dependence (equivalent to the one by Areias et al. [8]). Relevant data for this test is shown in Fig. 17. Here, the initial crack is explicitly represented (which was not in the original paper). Hardening law is inserted as a set of ordered pairs, as shown in Table 1. We monitor the force F as a function of the imposed displacement $\bar{v}$ and compare with the experimental results reported in Samal's paper. This compari-

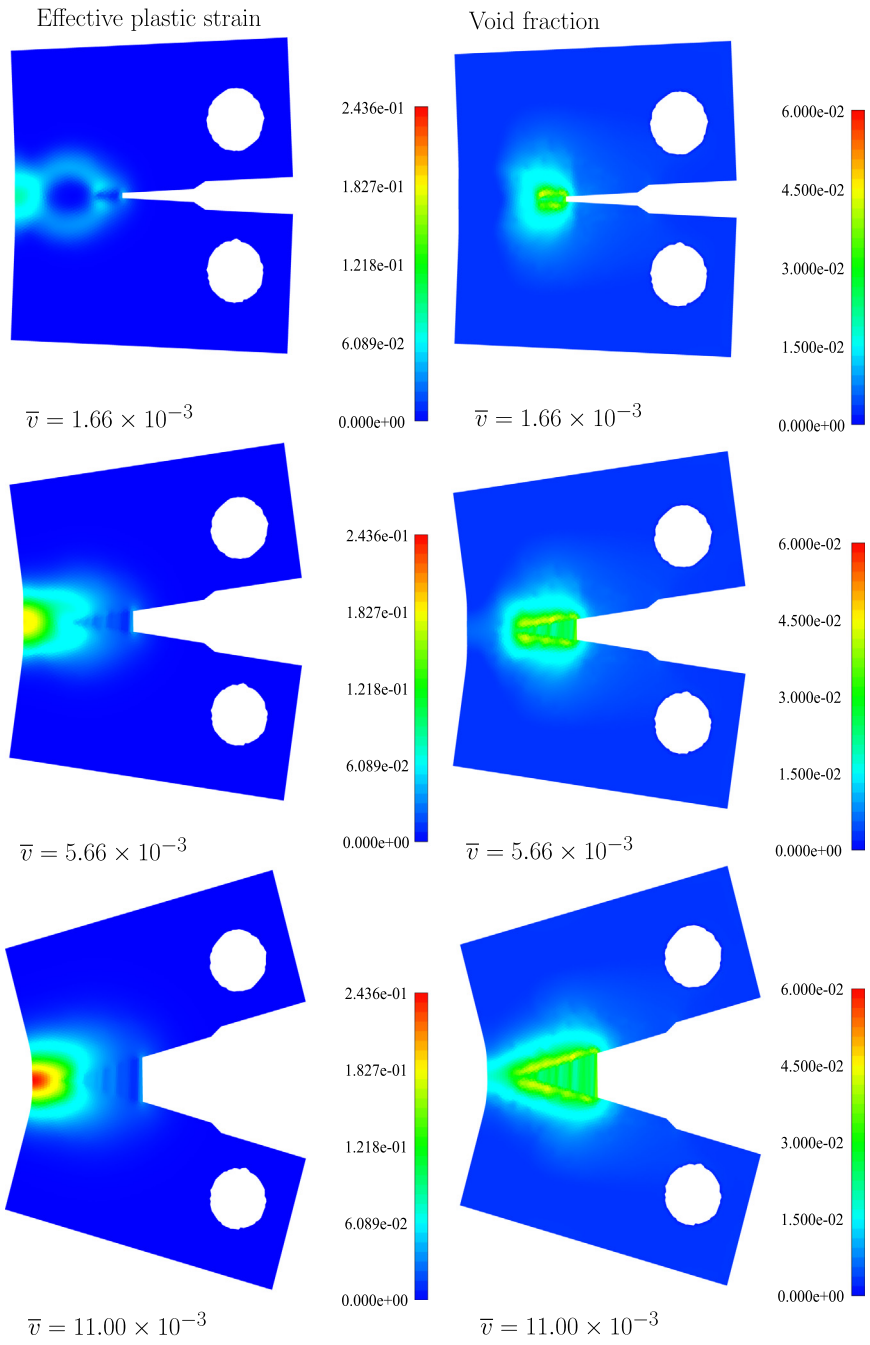

Fig. 19. Compact tension specimen (cf. [56]): sequence of effective plastic strain and void fraction contour plots.

son is presented in Fig. 18 where good agreement can be observed, despite the slightly higher values of reaction obtained here. Note that higher numerical values were also reported by Samal et al. [56]. A sequence of contour plots for the void fraction and effective plastic strain is shown in Fig. 19. Very high deformations are possible without convergence problems.

8. Conclusions

The combination of edge rotation algorithm with anisotropic element injection for computational fracture is advantageous from the implementation and generality perspective. Both quasi-brittle and ductile tests show that results are comparable to the tip remeshing algorithm proposed by the Authors (cf. [10,21,12,11,18]). We found that both for quasi-brittle and ductile fracture, classical benchmarks perform at least as well as competing techniques, with substantially fewer algorithmic steps. Recent enrichment techniques also show remarkable accuracy, but are more limiting for large amplitude displacements and the application to general elasto-plastic problems is not straightforward. If element erosion is adopted for ductile fracture problems (a typical approach in well-known commercial codes), the difference here is that a perfectly crack path is obtained, in contrast with the jagged path typical of erosion processes (cf. [63,66]). Additionally, unlike gradient or nonlocal methods [8], we have a energetically precise definition of the length scale. Concerning the characteristic length parameter θ, we found that the value 0.1 is acceptable, but other values have only a limited effect in the results. In the cup and cone fracture example, we noted a slight mesh dependence effect.

Acknowledgments

The authors gratefully acknowledge financing from the "Fundação para a Ciência e a Tecnologia" under the Project PTDC/EME-PME/108751 and the Program COMPETE FCOMP-01–0124-FEDER-010267.

References

[1] J. Alfaiate, A. Simone, L.J. Sluys, A new approach to strong embedded discontinuities, in: N. Bicanic, R. de Borst, H. Mang, G. Meschke (Eds.), Computational Modelling of Concrete Structures, EURO-C 2003, St. Johann im Pongau, Salzburger Land, Austria, March 2003.
[2] J. Alfaiate, G.N. Wells, L.J. Sluys, On the use of embedded discontinuity elements with crack path continuity for mode-I and mixed-mode fracture, Eng. Fract. Mech. 69 (2002) 661–686.
[3] S.S. Antman, Nonlinear Problems of Elasticity, second ed., Springer, 2005.
[4] P. Areias, Simplas. <https://ssm7.ae.illinois.edu:80/simplas>.
[5] P. Areias, Finite strain fracture of plates and shells, in: Congreso de Métodos Numéricos en Ingeniería, Bilbao, España, June 2013. SEMNI.
[6] P. Areias, T. Belytschko, Non-linear analysis of shells with arbitrary evolving cracks using xfem, Int. J. Numer. Methods Eng. 62 (2005) 384–415.
[7] P. Areias, T. Belytschko, Analysis of finite strain anisotropic elastoplastic fracture in thin plates and shells, J. Aerospace Eng. 19 (4) (2006) 259–270.
[8] P. Areias, J.M.A. César de Sá, Conceiçao António, A gradient model for finite strain elastoplasticity coupled with damage, Finite Elem. Anal. Des. 39 (2003) 1191–1235.
[9] P. Areias, J.M.A. César de Sá, C.A. Conceição António, J.A.S.A.O. Carneiro, V.M.P. Teixeira, Strong displacement discontinuities and Lagrange multipliers in the analysis of finite displacement fracture problems, Comput. Mech. 35 (2004) 54–71.
[10] P. Areias, D. Dias-da-Costa, J. Alfaiate, E. Júlio, Arbitrary bi-dimensional finite strain cohesive crack propagation, Comput. Mech. 45 (1) (2009) 61–75.
[11] P. Areias, D. Dias-da Costa, E.B. Pires, J. Infante Barbosa, A new semi-implicit formulation for multiple-surface flow rules in multiplicative plasticity, Comput. Mech. 49 (2012) 545–564.
[12] P. Areias, J. Garção, E.B. Pires, J. Infante Barbosa, Exact corotational shell for finite strains and fracture, Comput. Mech. 48 (2011) 385–406.
[13] P. Areias, T. Rabczuk, Quasi-static crack propagation in plane and plate structures using set-valued traction-separation laws, Int. J. Numer. Methods Eng. 74 (2008) 475–505.
[14] P. Areias, T. Rabczuk, Smooth finite strain plasticity with nonlocal pressure support, Int. J. Numer. Methods Eng. 81 (2010) 106–134.
[15] P. Areias, T. Rabczuk, Finite strain fracture of plates and shells with configurational forces and edge rotations, Int. J. Numer. Methods Eng. 94 (2013) 1099–1122.
[16] P. Areias, T. Rabczuk, D. Dias-da Costa, Element-wise fracture algorithm based on rotation of edges, Eng. Fract. Mech. 110 (2013) 113–137.
[17] P. Areias, M. Ritto-Corrêa, J.A.C. Martins, Finite strain plasticity, the stress condition and a complete shell model, Comput. Mech. 45 (2010) 189–209.
[18] P. Areias, H.G. Silva, N. Van Goethem, M. Bezzeghoud, Damage-based fracture with electro-magnetic coupling, Comput. Mech. 51 (2013) 629–640.
[19] P. Areias, J.-H. Song, T. Belytschko, A finite-strain quadrilateral shell element based on discrete kirchhoff-love constraints, Int. J. Numer. Methods Eng. 64 (2005) 1166–1206.
[20] P. Areias, J.-H. Song, T. Belytschko, Analysis of fracture in thin shells by overlapping paired elements, Comput. Method Appl. M. 195 (41-43) (2006) 5343–5360.
[21] P. Areias, N. Van Goethem, E.B. Pires, A damage model for ductile crack initiation and propagation, Comput. Mech. 47 (6) (2011) 641–656.
[22] D.N. Arnold, F. Brezzi, M. Fortin, A stable finite element for the Stokes equations, Calcolo XXI(IV), 1984, pp. 337–344.
[23] J. Besson, D. Steglich, W. Brocks, Modeling of crack growth in round bars and plane strain specimens, Int. J. Solids Struct. 38 (2001) 8259–8284.
[24] P. Betsch, E. Stein, Numerical implementation of multiplicative elasto-plasticity into assumed strain elements with application to shells at large strains, Comput. Method Appl. M. 179 (1999) 215–245.
[25] T.N. Bittencourt, A.R. Ingraffea, P.A. Wawrzynek, J.L. Sousa, Quasi-automatic simulation of crack propagation for 2D LEFM problems, Eng. Fract. Mech. 55 (2) (1996) 321–334.
[26] P. Bocca, A. Carpinteri, S. Valente, Mixed mode fracture of concrete, Int. J. Solids Struct. 27 (9) (1991) 1139–1153.
[27] B. Bourdin, G.A. Francfort, J.-J. Marigo, Numerical experiments in revisited brittle fracture, J. Mech. Phys. Solids 48 (2000) 797–826.
[28] O.T. Bruhns, A. Meyers, H. Xiao, On non-corotational rates of oldroyd's type and relevant issues in rate constitutive formulations, Proc. Roy. Soc. Lond. A Mater. 460 (2004) 909–928.
[29] E.W.V. Chaves, PhD thesis, Universitat Politècnica de Catalunya, Escola Tècnica Superior D'Enginyers de Camins, Canals I Ports, Barcelona, Spain, February 2003.
[30] B. Chen, P.T. Harker, Smooth approximations to nonlinear complementarity problems, SIAM J. Optim. 7 (2) (1997) 403–420.
[31] C. Chen, O.L. Mangasarian, A class of smoothing functions for nonlinear and mixed complementarity problems, Comput. Optim. Appl. 5 (1996) 97–138.
[32] D. Colombo, M. Giglio, A methodology for automatic crack propagation modelling in planar and shell fe models, Eng. Fract. Mech. 73 (2006) 490–504.
[33] C. Comi, L. Driemeier, Material Instabilities in Solids, John Wiley and Sons, 1998 (Chapter 26).
[34] D. Dias-da-Costa, J. Alfaiate, L.J. Sluys, E. Júlio, A discrete strong discontinuity approach, Eng. Fract. Mech. 76 (9) (2009) 1176–1201.
[35] J. Dolbow, N. Moës, T. Belytschko, Modeling fracture in Mindlin–Reissner plates with the extended finite element method, Int. J. Solids Struct. 37 (2000) 7161–7183.
[36] A.L. Eterovic, K.J. Bathe, On the treatment of inequality constraints arising from contact conditions in finite element analysis, Comput. Struct. 40 (2) (1991) 203–209.
[37] G. Etse, K. Willam, Failure analysis of elastoviscoplastic material models, J. Eng. Mech. – ASCE 125 (1999) 60–69.
[38] A. Hansbo, P. Hansbo, A finite element method for the simulation of strong and weak discontinuities in solid mechanics, Comput. Method Appl. M. 193 (2004) 3523–3540.
[39] G.A. Holzapfel, Nonlinear Solid Mechanics: A Continuum Approach for Engineers, John Wiley and Sons, 2000.
[40] T.J.R. Hughes, The Finite Element Method, Dover Publications, 2000. Reprint of Prentice-Hall edition, 1987.
[41] B.L. Karihaloo, Q.Z. Xiao, Modelling of stationary and growing cracks in FE framework without remeshing: a state-of-the-art review, Comput. Struct. 81 (2003) 119–129.
[42] J. Korelc, Multi-language and multi-environment generation of nonlinear finite element codes, Eng. Comput. 18 (4) (2002) 312–327.
[43] G. Legrain, N. Moës, E. Verron, Stress analysis around crack tips in finite strain problems using the extended finite element method, Int. J. Numer. Methods Eng. 63 (2005) 290–314.
[44] S. Loehnert, T. Belytschko, A multiscale projection method for macro/microcrack simulations, Int. J. Numer. Methods Eng. 71 (2007) 1466–1482.
[45] C. Miehe, E. Gürses, A robust algorithm for configurational-force-driven brittle crack propagation with *r*-adaptive mesh alignment, Int. J. Numer. Methods Eng. 72 (2007) 127–155.
[46] N. Moës, T. Belytschko, Extended finite element method for cohesive crack growth, Eng. Fract. Mech. 69 (2002) 813–833.
[47] N. Moës, J. Dolbow, T. Belytschko, A finite element method for crack growth without remeshing, Int. J. Numer. Methods Eng. 46 (1999) 131–150.
[48] R.W. Ogden, Non-linear Elastic Deformations, Dover Publications, Mineola, New York, 1997.
[49] J. Oliver, A consistent characteristic length for smeared cracking models, Int. J. Numer. Methods Eng. 28 (1989) 461–474.
[50] J. Oliver, Continuum modelling of strong discontinuities in solid mechanics using damage models, Comput. Mech. 17 (1995) 49–61.
[51] T. Rabczuk, P. Areias, A meshfree thin shell for arbitrary evolving cracks based on an external enrichment, Comput. Model Eng. Sci. 16 (2) (2006) 115–130.
[52] T. Rabczuk, P. Areias, T. Belytschko, A meshfree thin shell method for non-linear dynamic fracture, Int. J. Numer. Methods Eng. 72 (2007) 524–548.
[53] T. Rabczuk, T. Belytschko, Cracking particles: a simplified meshfree method for arbitrary evolving cracks, Int. J. Numer. Methods Eng. 61 (2004) 2316–2343.
[54] A. Rodríguez-Ferran, I. Morata, A. Huerta, A new damage model based on nonlocal displacements, Int. J. Numer. Methods Eng. 29 (5) (2005) 473–493.
[55] G. Rousselier, Ductile fracture models and their potential in local approach of fracture, Nucl. Eng. Des. 105 (1987) 97–111.
[56] M.K. Samal, M. Seidenfuss, E. Roos, A new mesh-independent Rousselier's damage model: finite element implementation and experimental verification, Int. J. Mech. Sci. 51 (2009) 619–630.
[57] E. Samaniego, T. Belytschko, Continuum-discontinuum modelling of shear bands, Int. J. Numer. Methods Eng. 62 (13) (2005) 1857–1872.
[58] E. Samaniego, X. Oliver, A. Huespe. Contributions to the continuum modelling of strong discontinuities in two-dimensional solids, in: Monograph CIMNE 72, International Center for Numerical Methods in Engineering, Barcelona, Spain, 2003.
[59] E. Schlangen, Experimental and numerical analysis of fracture processes in concrete, PhD thesis, Delft, 1993.
[60] H.L. Schreyer, Z. Chen, One-dimensional softening with localization, J. Appl. Mech. – ASME 53 (1986) 791–797.
[61] J.C. Simo, T.J.R. Hughes, Computational Inelasticity, corrected second printing ed., Springer, 2000.
[62] M.A. Sutton, X. Deng, F. Ma, J.C. Newman Jr., M. James, Development and application of a crack tip opening displacement-based mixed mode fracture criterion, Int. J. Solids Struct. 37 (2000) 3591–3618.
[63] X. Teng, T. Wierzbicki, Evaluation of six fracture models in high velocity perforation, Eng. Fract. Mech. 73 (2006) 1653–1678.
[64] C. Truesdell, W. Noll, The Non-linear Field Theories of Mechanics, third ed., Springer, 2004.
[65] N. Van Goethem, P. Areias, A damage-based temperature-dependent model for ductile fracture with finite strains and configurational forces, Int. J. Fract. 178 (2012) 215–232.
[66] L. Xue, T. Wierzbicki, Ductile fracture initiation and propagation modeling using damage plasticity theory, Eng. Fract. Mech. 75 (2008) 3276–3293.